C. R. Physique 15 (2014) 705–718

Contents lists available at ScienceDirect

Comptes Rendus Physique

www.sciencedirect.com

Liquid and solid foams / Mousses liquides et solides

On the creep deformation of nickel foams under compression

Déformation par fluage de mousses de nickel sous contrainte de compression

Anthony Burteau, Jean-Dominique Bartout, Yves Bienvenu, Samuel Forest *

MINES ParisTech, Centre des matériaux, CNRS UMR 7633, BP 87, 91003 Évry cedex, France

ARTICLE INFO

Article history:
Available online 3 October 2014

Keywords:
Nickel foam
Creep
Microtomography
Open cell foam
Viscoplasticity
Buckling

Mots-clés :
Mousse de nickel
Fluage
Microtomographie
Mousse à cellules ouvertes
Viscoplasticté
Flambage

ABSTRACT

A finite-element computational strategy is developed to study the viscoplastic deformation mechanisms at work in a nickel foam sample under compression creep. The constitutive law for pure nickel accounts for both diffusional and dislocation creep mechanisms. The finite-element results show the competition between both mechanisms due to the strong heterogeneity of the stress distribution in the foam. The initiation of the viscoplastic buckling phenomenon leading to cell crushing in tertiary creep is illustrated. The overall model prediction is compared to the results of compression creep tests performed in vacuo at 900 °C.

RÉSUMÉ

Une stratégie de calcul par éléments finis a été développée dans le but d'étudier les mécanismes de déformation viscoplastique à l'oeuvre dans une mousse de nickel sous fluage en compression. La loi de comportement du nickel pur intègre à la fois les mécanismes de fluage diffusionnel et de fluage-dislocations. Les résultats des calculs par éléments finis font apparaître une compétition entre ces deux mécanismes du fait de la forte hétérogénéité de la distribution des contraintes dans la mousse. L'initiation du phénomène de flambage viscoplastique aboutissant à l'écrasement des cellules en fluage tertiaire est illustrée. La réponse globale obtenue à l'aide du modèle est comparée aux résultats d'essais de fluage en compression réalisés sous vide à 900 °C.

1. Introduction

The creep of foams has been the subject of numerous studies initiated by [1] and dedicated to syntactic [2] and metallic foams [3,4]. The first contributions tackle the problem of creep modelling for cellular solids based on a simple

* Corresponding author. Tel.: +33 1 60 76 30 51; fax: +33 1 60 76 31 50.
E-mail address: samuel.forest@ensmp.fr (S. Forest).

http://dx.doi.org/10.1016/j.crhy.2014.09.004
1631-0705/

two-dimensional approach [5], and more recently on more sophisticated homogenization methods [6]. Idealized unit cell models are used as simple tools to understand the possible mechanisms at work in open cell foams undergoing creep [7]. The objective is to understand how the applied overall stress redistributes in the parts of the foam and to investigate whether the induced strong heterogeneity in stress is detrimental or not for the otherwise outstanding properties of metallic foams. Periodic microstructures like 2D honeycombs [8] and 3D hollow-sphere structures under creep [9,10] can be used to identify the creep mechanisms and associated failure modes. Creep failure mechanisms corresponding to the beginning of tertiary creep were identified as viscoplastic buckling of struts in open-cell foams or walls and junctions in closed cell foams in [11–13], based on idealized cell morphologies like a pentagonal dodecahedron cell geometry. More elaborate modelling relies on creep simulation of large material volume elements taking into account the random structure of the foam, for instance in the case of ice foam [14].

The objective of the present work is to discuss the creep deformation modes at work in open-cell nickel foams used for battery or filtering applications. The material processing of this kind of foams was described in [15]. The morphology of the cell distribution and its size was studied in detail in [16] by means of computed microtomography and the corresponding systematic image analysis delivering a statistical description of cell population. Due to the existence of a polymeric precursor in the processing of the nickel foam, the struts are hollow beams with typical plateau border cross-sections. As a result, the nickel grains in the 10-μm thin walls of the struts form a bamboo structure with columnar grains. The effect of grain size on the tensile behaviour of these foams at room temperature was investigated in [17].

The macroscopic creep properties of nickel foams and a first insight into deformation mechanisms in the cells were provided in [7,18,19]. The effects of strut geometry and pore fraction were evidenced in [20]. These works serve as a basis for the analysis of the creep of nickel-based superalloy foams [21], more readily suitable for high-temperature applications due to oxidation. The tensile creep behaviour of the nickel foam was studied in [18], and the present work deals with the case of compression creep.

The importance of microtomography in deciphering the deformation and damage mechanisms of foams must be underlined [22,23]. The obtained images serve as the starting point for a finite-element computational approach of the mechanics of closed-cell foams [22,24,25] and [7,18] for open-cell nickel foams. The computational strategy defined in [26] for the design of optimal foams with targeted mechanical properties is applied in the present work to analyse the compression creep mechanisms of nickel foams. In particular, it has been shown in [26] how high-performance finite-element computing can be used to design optimal cell morphology regarding the anisotropy of mechanical tensile properties. This computational strategy is further developed in the present work to explore the creep deformation mechanisms in nickel foams from a computational perspective, as done for instance in [27] for the multiaxial creep of low-density open-cell foams.

The attention is focused on the competition between diffusional and dislocation creep mechanisms that will be shown to be simultaneously activated in the foam due to the tremendous heterogeneity of the stress in the microstructure. The computational approach is validated by means of compression creep tests at high temperature under vacuum to avoid oxidation. The considered nickel foams are produced in the form of 1.5-mm thick sheets and compression creep is applied within the thickness of the foam samples. In order to optimize the creep test conditions, some monotonic compression tests were performed to determine the stress levels to be used during creep experiments and the deformation values for creep failure. These values depend on foam cell shape and size. After this threshold value is reached, the foam structure collapses and the creep rate strongly increases [28].

The prediction of creep behaviour through a computational homogenization method requires a detailed knowledge of the constitutive behaviour of pure nickel, which is the subject of Section 2, where literature results are compiled. A constitutive elastoviscoplasticity model for pure nickel is formulated, including the diffusional and dislocation creep deformation mechanisms and the corresponding material parameters are identified. The experimental part of the work is presented in Section 3. The finite-element results are reported in Section 4. They include the design of a finite-element mesh of a group of about 30 cells and the distributions of stress and viscoplastic strain during creep at a low stress and at a high stress level. They are discussed in Section 5 focusing on the comparison between predicted and experimental creep curves.

Regarding notations, symmetric second-order tensors are denoted by a tilde, like for instance the stress tensor, $\underset{\sim}{\boldsymbol{\sigma}}$. The time derivative of a second-order tensor is written $\dot{\underset{\sim}{\boldsymbol{\varepsilon}}}$.

2. Creep of pure nickel

The creep behaviour of polycrystalline pure nickel is heavily dependent on temperature and stress levels. At low temperature or, equivalently, at large stresses, viscoplastic deformation is governed by the slip of dislocations. At higher temperatures, the stress level dictates the viscoplastic deformation mechanism. Relatively high stresses lead to dislocation creep mediated by bulk vacancy diffusion or by pipe-diffusion along dislocation cores. Low stresses induce diffusion creep resulting from the motion of vacancies in the bulk or along grain boundaries [29].

2.1. Compiling results from literature

Deformation mechanism maps, as available in [30], can be drawn in the space of normalised shear stress and homologous temperature, for a given grain size. The typical limits of the domain of diffusional flow, power-law creep and plasticity are

Table 1
Typical values of the activation energy and Norton exponent for the creep of bulk polycrystalline pure nickel depending on temperature and applied stress [31]. The initial yield stress at room temperature is denoted by σ_0.

	$\sigma \ll \sigma_0$	$\sigma \leq \sigma_0$	$\sigma > \sigma_0$
$T > 0.8\,T_m$	$n = 1$; $Q = 275$–280 kJ/mol	$n = 4.6$; $Q = 275$–280 kJ/mol	–
$0.55\,T_m < T < 0.8\,T_m$	$n = 1$; $Q = 115$ kJ/mol	$n = 4.6$; $Q = 275$–280 kJ/mol	–
$0.3\,T_m < T < 0.55\,T_m$	–	$n = 6.6$; $Q = 170$ kJ/mol	–
$T < 0.3\,T_m$	–	–	$n = 2$

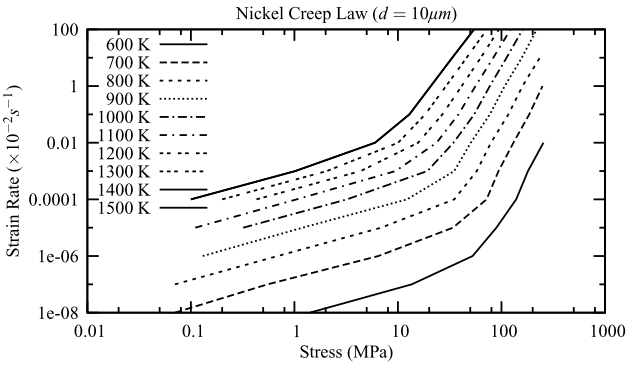

Fig. 1. Strain rate/stress maps for creep of polycrystalline bulk nickel over a wide range of temperatures.

taken from Ashby's map for pure nickel with a grain size $d = 10$ μm, which is the typical value in the struts of the nickel foams considered in this work [15,17].

A detailed review of the creep behaviour of bulk pure nickel and in the form of films can be found in [31]. In particular, the values of the activation energy Q for dislocation creep, bulk or grain boundary diffusion creep, and of the Norton exponent n for power-law creep are discussed in [32,33] for bulk polycrystalline nickel over a large temperature range. These values are summarized in Table 1. The creep responses as read from Ashby's maps as a function of stress are plotted in Fig. 1 for a large range of temperatures and for the grain size $d = 10$ μm. These curves clearly show the two creep regimes at low and high stress levels and the transition zones where both diffusion and dislocation mechanisms are simultaneously activated.

As a result of the processing route based on a polymer precursor, the nickel foams studied in [15,16,26] are made of hollow struts with typically 10-μm thick walls. These walls are therefore thin films made of columnar grains with in-plane grain size of 5 to 20 μm. A detailed study of the effects of grain size on the behaviour of nickel films and nickel foams [17] clearly shows that nickel films behave in a way significantly different than bulk nickel, at least under tension loading. Experimental results for the creep behaviour of nickel films remain scarce and mainly deal with their oxidation under creep [34]. In nickel films with the same grain size [17], crystallographic texture and columnar morphology as in the strut walls of our open-cell nickel foams were produced and tested mechanically under monotonic tensile loading, mainly at room temperature. The found properties were used to predict the response of the foam based on 3D microtomographic images and corresponding finite-element analyses in [26]. However, nickel films were not tested under creep under oxygen-free atmosphere, so that we cannot compare their creep response to the bulk properties previously listed. Accordingly, the latter will be used in the micromechanical simulations of Section 3.

2.2. Identification of the viscoplastic constitutive model for pure nickel

The constitutive model used in this work for pure nickel includes two inelastic deformation mechanisms associated with diffusional and dislocation creep:

$$\underset{\sim}{\boldsymbol{\varepsilon}} = \underset{\sim}{\boldsymbol{\varepsilon}}^{e} + \underset{\sim}{\boldsymbol{\varepsilon}}^{v}_{diff} + \underset{\sim}{\boldsymbol{\varepsilon}}^{v}_{disl} \tag{1}$$

where $\underset{\sim}{\boldsymbol{\varepsilon}}$ and $\underset{\sim}{\boldsymbol{\varepsilon}}^{e}$ are the total strain tensor and the elastic strain tensor, respectively. Diffusion (resp. dislocation) creep is accounted for by means of the strain $\underset{\sim}{\boldsymbol{\varepsilon}}^{v}_{diff}$ (resp. $\underset{\sim}{\boldsymbol{\varepsilon}}^{v}_{disl}$). The decomposition of the total strain into several viscoplastic contributions belongs to the class of multi-mechanisms plasticity models as initially proposed by Mandel and explored in [35,36]. The viscoplastic strain rates follow from the following flow rules:

$$\dot{\underset{\sim}{\boldsymbol{\varepsilon}}}^{v}_{diff} = \dot{v}_{diff} \frac{\underset{\sim}{\boldsymbol{\sigma}}^{dev}}{J_2(\underset{\sim}{\boldsymbol{\sigma}})} \quad \text{with } \dot{v}_{diff} = \left\langle \frac{J_2(\underset{\sim}{\boldsymbol{\sigma}}) - R_{0diff}}{K_{diff}} \right\rangle^{n_{diff}} \tag{2}$$

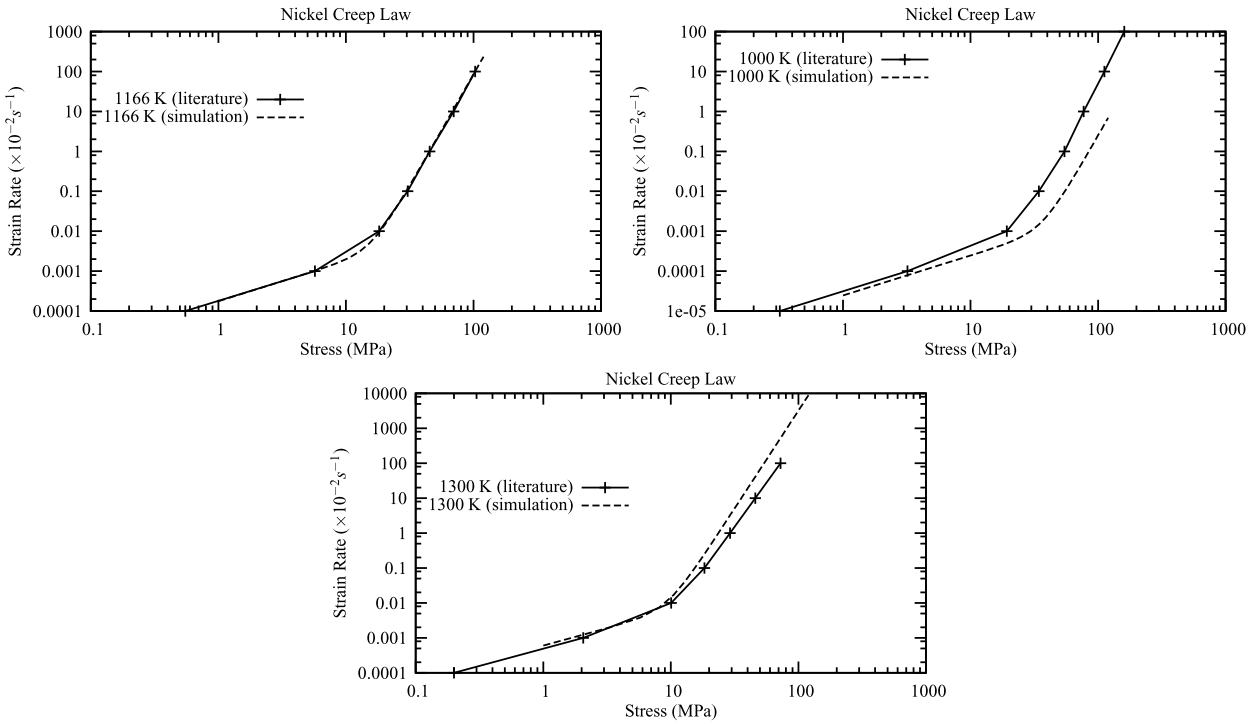

Fig. 2. Comparison between literature data and model prediction for the creep of pure nickel at three temperatures.

$$\dot{\underset{\sim}{\varepsilon}}^{\mathrm{v}}_{\mathrm{disl}} = \dot{\nu}_{\mathrm{disl}} \frac{\underset{\sim}{\sigma}^{\mathrm{dev}}}{J_2(\underset{\sim}{\sigma})} \quad \text{with } \dot{\nu}_{\mathrm{disl}} = \left\langle \frac{J_2(\underset{\sim}{\sigma}) - R_{0\mathrm{disl}}}{K_{\mathrm{disl}}} \right\rangle^{n_{\mathrm{disl}}} \tag{3}$$

where $\underset{\sim}{\sigma}^{\mathrm{dev}}$ is the deviatoric part of the stress tensor $\underset{\sim}{\sigma}$. The von Mises equivalent stress is $J_2(\underset{\sim}{\sigma}) = \sqrt{3/2 \underset{\sim}{\sigma}^{\mathrm{dev}} : \underset{\sim}{\sigma}^{\mathrm{dev}}}$. The brackets are defined as $\langle \bullet \rangle = \mathrm{Max}(0, \bullet)$. The material parameters of the viscoplastic model are the exponents $n_{\mathrm{diff}}, n_{\mathrm{disl}}$ and the viscosity coefficients $K_{\mathrm{diff}}, K_{\mathrm{disl}}$ with temperature dependence follow an Arrhenius law in the form:

$$\frac{1}{K_{\mathrm{diff}}^{n_{\mathrm{diff}}}} = A_{\mathrm{diff}} \exp\left(-\frac{Q_{\mathrm{diff}}}{RT}\right), \qquad \frac{1}{K_{\mathrm{disl}}^{n_{\mathrm{disl}}}} = A_{\mathrm{disl}} \exp\left(-\frac{Q_{\mathrm{disl}}}{RT}\right) \tag{4}$$

with the values $A_{\mathrm{diff}} = 0.05$ MPa s^{-1} and $A_{\mathrm{disl}} = 0.4$ MPa s^{-1}. The computations will be performed at the temperature $T = 900\,^{\circ}\mathrm{C}$, for which $n_{\mathrm{diff}} = 1, n_{\mathrm{disl}} = 6.6$.

The elastic strain tensor is related to the stress tensor by Hooke's law in the isotropic case with the following temperature dependence of Young's modulus:

$$E(T) = E_0 \left(1 - \alpha \frac{T - 300}{T_{\mathrm{m}}}\right) \tag{5}$$

with the room temperature Young's modulus $E_0 = 204$ GPa [37], the melting temperature T_{m} and $\alpha = 0.64$ [30]. At $T = 900\,^{\circ}\mathrm{C}$, which is the temperature retained for the simulations, we have $E = 139$ GPa. The Poisson ratio is taken as $\nu = 0.3$.

The creep strain rates depending on the applied stress, as predicted according to this model, are given in Fig. 2 for three temperatures. They reproduce satisfactorily the curves deduced from Ashby's map (see Fig. 1) that are superimposed to the graphs. These curves exhibit the two creep regimes at low and high stress levels and the transition zones where both diffusion and dislocation mechanisms are activated.

The presented viscoplastic model is implemented in the 3D finite-element code Z-set [38] that will be used in the following simulations. It represents the mechanical model for the constitutive material of the nickel foams.

3. Creep of nickel foams

3.1. Tested material and experimental setup

The tested material is a nickel foam with relative density 7.4% and a pore size of 580 µm. The foam is produced in the form of sheets with a thickness $h = 1.5$ mm. Small square samples were compressed in the normal direction to the foam

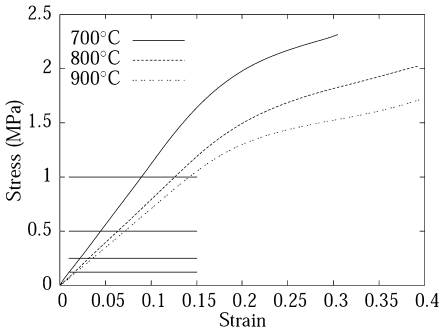

Fig. 3. Monotonic compression curves of the nickel foam at three different temperatures at a strain rate of 10^{-3} s^{-1}. The horizontal lines indicate the stress levels selected for the creep tests.

sheet. Three testing temperatures were retained: 700 °C, 800 °C and 900 °C, which are close to the target temperatures for DPF applications [18].

The compression creep tests were performed on 20 mm × 20 mm square specimens with 1.5-mm thickness, under secondary vacuum (10^{-5} mbar) to avoid oxidation that dramatically affects the mechanical properties of nickel at the considered temperatures. The water-cooled load cell, the radiant heater and the mechanical assembly are included inside the vacuum chamber. The displacement of the interior grip is prescribed by an electro-mechanical actuator outside the chamber, which can be load or displacement controlled. The sample and the whole mechanical assembly are heated in a four-lobe radiant heater. A temperature regulator (Eurotherm type) controls the electric power of the heater. A Pt/Pt–Rh10% thermocouple is spot-welded on one of the two compression plates, near the foam sample [28]. All the mechanical components are made of Inconel 718. Owing to the significant mass of the mechanical assembly to be heated, a period of about half an hour is necessary to stabilize the temperature before starting a mechanical test. The targeted stresses and the sample dimensions require rather low loads, from 10 to 1000 N. A conventional extensometer with mechanical contacts would affect the load applied to the sample and the load measurement. That is why we used a laser beam extensometer. Its accuracy is about 0.1 µm and its full range is 50 mm. This extensometer is located outside the vacuum chamber and the laser beam passes through two windows, which are transparent to near-red-range light wavelengths. Some grooves are machined on the lines and the extensometer measures the relative displacement of the two grooves. During the heating, a very low load is applied on the sample and a variation of the signal is then observed because of the thermal expansion of the materials (nickel and Inconel 718). But, during isothermal operations, the signal variation corresponds only to the foam thickness variation. During an experiment, temperature, the relative displacement of the compression plates (ΔL) and applied load (F) are continuously recorded. These values are used to determine the strain ($\Delta L/L_0$), and the stress (F/S_0).

The samples have been taken from delivered A4 foam sheets with a cut-off wheel with low cutting feed, but the consequence of such process is that the foam struts at the boundary of the sample are deformed. So, each machined side of the sample has been ground with 600 abrasive SiC paper. The sample dimensions have been measured with a numerical caliper with an accuracy of 0.02 mm. The weight of each sample is also measured in order to determine its relative density. The dispersion of the sample population is about 5%, making the experimental conditions reproducible from an experiment to another. The foam sheets are not fully planar. Then, small bumps can affect the measurement of the stress because the initial contact surface with the compressive plates is unknown and smaller than the measured surface (S_0). Reliable strain rates cannot be measured for stress levels below 0.1 MPa with our equipment.

The heating rate has been fixed at 150 °C per minute. During the pumping, heating and temperature stabilizing periods before mechanical testing, the applied load will be fixed at 10 N, which is sufficient to maintain the sample, but not enough to deform significantly the foam before testing. For the monotonic compressive tests, the actuator speed is set to 1.7 mm/min, which means that the initial strain rate is about 10^{-2} s^1.

3.2. Experimental results

Typical monotonic compression curves at a strain rate of 10^{-3} s^{-1} are given in Fig. 3 for the three temperatures. The test is interrupted when the deformation of foam exceeds 40% or the stress level reaches 2.5 MPa. The curves are truncated before significant densification. They display a long quasi-linear stage followed by generally monotonic hardening, even though an inflexion point is observed at 900 °C. This is in contrast to the compression curves for lower relative densities, which exhibit a stress peak and a plateau prior to densification. The quasi-linear regime should not be interpreted as an elastic domain since irreversible deformation can be shown to occur when the sample is unloaded in this regime. The monotonic character of the curve is correlated with the absence of crushing bands observed in this rather dense nickel foam. Low stress levels were selected for the creep tests to avoid catastrophic buckling of the struts: 0.12, 0.25, 0.50, and 1 MPa. They are reported on the compression curves of Fig. 3 and are located in the quasi-linear regime.

The four previous load levels were prescribed on the same specimen at a given temperature, jumping from one stress value to the other once a clear steady-state regime was reached for each stress level. Prior to this test campaign, it was

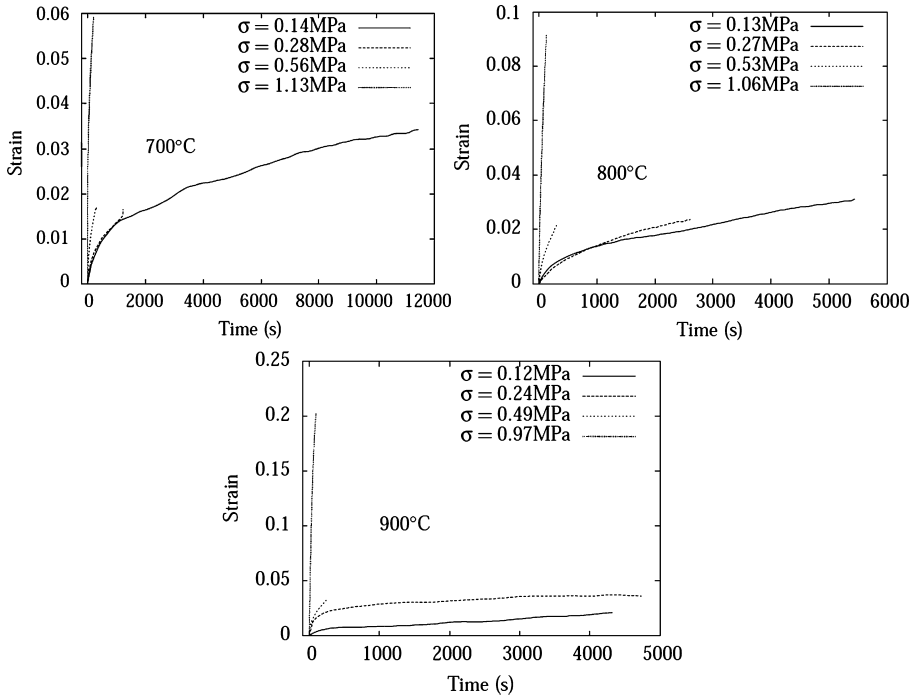

Fig. 4. Creep test results at three temperatures and at four stress levels.

Table 2
Stationary creep rates measured for the compression of nickel foams at 3 temperatures and 4 stress levels.

700 °C		800 °C		900 °C	
0.14 MPa	1.09×10^{-6} s^{-1}	0.13 MPa	3.03×10^{-6} s^{-1}	0.12 MPa	2.80×10^{-6} s^{-1}
0.28 MPa	6.66×10^{-6} s^{-1}	0.27 MPa	5.88×10^{-6} s^{-1}	0.24 MPa	3.62×10^{-6} s^{-1}
0.56 MPa	3.07×10^{-5} s^{-1}	0.53 MPa	4.92×10^{-5} s^{-1}	0.49 MPa	7.46×10^{-5} s^{-1}
1.13 MPa	1.40×10^{-4} s^{-1}	1.06 MPa	5.41×10^{-4} s^{-1}	0.97 MPa	1.15×10^{-3} s^{-1}

checked that the material's behaviour does not exhibit memory effects at these temperatures. The cumulative strain undergone by each sample did not go beyond 10%, corresponding to the upper limit of the quasi-linear part of the compression curves of Fig. 3. The reproducibility of the test results was checked. Individual creep curves were extracted from each complete test for each stress level. The corresponding creep curves are shown in Fig. 4. Primary creep is visible on each curve, whereas a clear secondary creep stage can be defined in most cases. The stationary creep rates were computed at the end of the presented curves and the found values are gathered in Table 2. The representation of these results in the log–log diagram of Fig. 5 shows two domains of power-law creep at the two highest temperatures and almost one single regime at the lowest temperature.

The constitutive model presented in Section 2.2 can be simplified in the case of uniaxial creep and neglecting elastic strain, in the form:

$$\dot{\varepsilon} = K_1 \sigma^{n_1} + K_2 \sigma^{n_2}, \quad K_2 = k_2 \exp\left(-\frac{Q}{RT}\right) \tag{6}$$

Stress and strain σ and ε refer to the opposite values of the uniaxial compression stress and strain components. The following values of the coefficients and activation energy are identified: $K_1 = 2.31 \times 10^{-5}$ MPa^{-1} s^{-1}, $k_2 = 232$ MPa$^{-n_2}$ s^{-1}, $Q = 14{,}150R$, $n_1 = 1$, $n_2 = 9.2 \times 10^{-3}T - 6.615$. The latter interpolation corresponds to $n_2 = 2.3$ at 700 °C, $n_2 = 3.3$ at 800 °C and $n_2 = 4.2$ at 900 °C. The predicted strain rates based on the identified parameters and for a large range of stresses are illustrated in Fig. 6 and can be directly compared to the experimental results of Fig. 5. The transition from the domain of diffusion creep to a more general power law creep is located around $\sigma = 0.24$ MPa.

The objective of the next section is to see whether the micromechanical approach is able to predict the observed macroscopic creep behaviour.

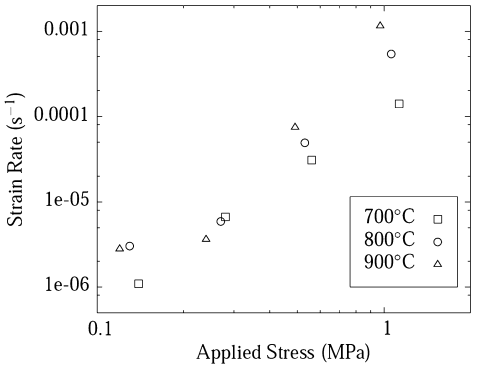

Fig. 5. Log–log representation of the stationary creep strain rates at three temperatures and four stress levels for nickel foams.

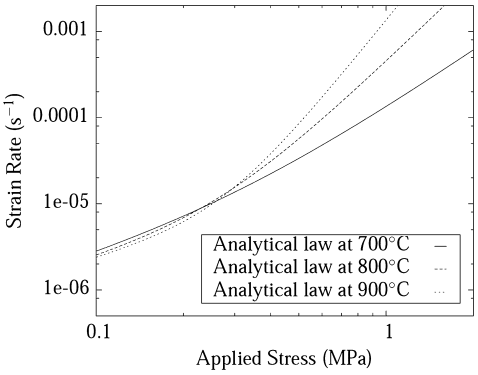

Fig. 6. Creep laws identified for nickel foams: three different temperatures show the transition from diffusional to dislocation creep.

4. 3D finite-element computation of nickel foam creep

Based on the constitutive behaviour of pure nickel, 3D representative images of the foam microstructure are used to predict the overall compression creep response and the deformation mechanisms in the struts and nodes of the foam. High-temperature in situ microtomographic imaging of creep tests could not be performed within this project, even though first results exist for other types of materials and testing [39]. The computations of this work are based on predictive simulations considering a representative foam sample generated in a way described in the first subsection.

4.1. Design of a virtual foam image and corresponding finite-element mesh

The prediction capabilities of finite-element simulations based on 3D microtomographic images have been demonstrated for the elastoplasticity of nickel foams in tension at room temperature in [26]. It is now extended to the case of creep loading at high temperatures. No microtomographic image of the nickel foam with 7.5% relative density used in the previous experiments was available. We have therefore developed a design methodology of virtual foam microstructures starting from microtomographic image of the polymeric foam precursor. The designed image treatment mimics the real processing of the nickel foam described in detail in [26]. Images of the PU precursor foams and corresponding finite-element mesh can be found in the latter reference. One of them with size $1.5 \times 1.5 \times 1.5$ mm^3 containing the whole thickness of the sample is selected. A dilation treatment is applied to the material part of the black-and-white image of the PU foam and the initial image is subtracted from the dilated image, so as to obtain a 7.5% dense foam with hollow struts. The removal of the PU skeleton reproduces the burning of the polymer during the heat treatment applied to the foams in the real processing. Note that a deformation of 7% in the so-called RD direction (see [26] for the definition of the material frame RD, TD, ND) was applied to the initial PU image, which mimics the fact that the foam sheets are subjected to a tensile force during the electrolytic deposition and heat treatment, which leads to elastic deformation of the PU foam and finally irreversible straining of the nickel foam. The associated lateral contractions were also applied to the image as an overall homogeneous deformation. A 3D volumic finite-element mesh is built based on the final image following a procedure described in [26]. Note that the procedure starts with a fine meshing of the inner and outer surface of the cells, providing smooth free surfaces. The thickness of the strut and node walls are then meshed by 3D volume finite elements. The obtained mesh contains 500,000 nodes, i.e. 1.5 million degrees of freedom. The cuboidal volume contains about 30 complete or incomplete cells and the whole thickness of the sample is included in the mesh, which corresponds to about three cells, see the finite-element mesh of Fig. 7.

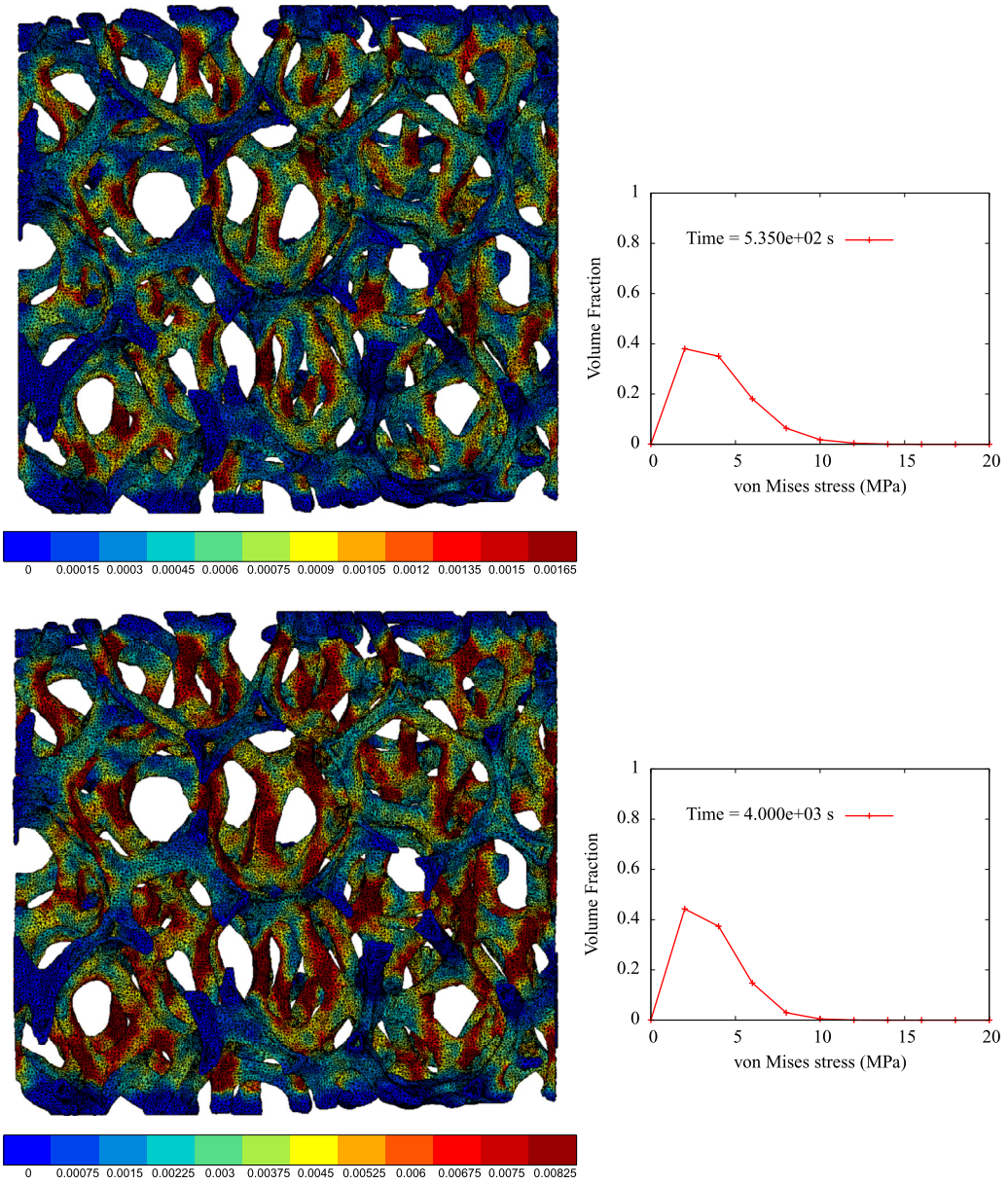

Fig. 7. (Colour online.) Field of cumulative plastic strain v_{diff} (left) inside the foam sample, and distribution of the equivalent von Mises stress within the foam (right) for a creep stress $\sigma = 0.12$ MPa applied to the foam. The top and bottom rows correspond to the creep time steps $t = 535$ s and $t = 4000$ s, respectively.

The results of the simulation of two creep tests are presented in the two next subsections corresponding to two strongly different stress levels. The boundary conditions prescribed to simulate the creep test on this small volume of metallic foam are the following. A vanishing vertical displacement (through-thickness direction) component U_3 is imposed to the group of nodes at the bottom of the mesh. These nodes are located at the cross section between some struts of the foam and the bottom plane surface. These nodes lie in a single plane up to a small tolerance due to the fact that nickel foam upper and lower surfaces are intrinsically rough. The upper plane of the mesh constitutes a similar planar set of nodes for which the vertical displacement U_3 is subjected to the linear multi-point constraint that all the nodes must share the same value of U_3 at each time step. As a result, there is only one unknown for the vertical displacement of all the nodes belonging to the upper plane. A force is then applied to one node of this group, which amounts to imposing the total vertical force applied to the foam. This force is computed from the targeted creep stress multiplied by the initial surface of this face of the cuboidal foam element. The force is first increased from 0 to the wanted force level and then maintained constant with time.

Accordingly, we do not simulate the contact conditions between the upper and lower parts of the foam and the plateaus of the compression machine. This simplification may have some consequences on the beginning of the creep curve since, in the experiment, the contact between all abutting struts and the machine plates is not instantaneously achieved.

The simulations are performed within the large deformation framework based on the corotational frame concept [36] and using the constitutive equations and material parameters determined in Section 2.

4.2. Strain heterogeneities at a low compression stress

The virtual metallic foam sample is first subjected to a low overall compressive stress level of 0.12 MPa at the temperature of 900 °C. The complex architecture of the foam leads to a complex distribution of stresses inside the struts and the nodes of the cells. The right column of Fig. 7 gives the histogram of the distribution of the von Mises equivalent stress at all Gauss points of the nickel mesh. It appears that the small overall load generates equivalent stresses with a mean value of about 4 MPa in the metal with a large variance. The local stresses remain however mostly below 10 MPa, which is the domain of diffusional creep for pure nickel, as shown in Fig. 2. After 4000 s, the stress distribution significantly changed and displays a lower variance. Maximal stress values go below 10 MPa and the number of points subjected to 2 to 4 MPa has increased. This corresponds to a stress relaxation taking place in different parts of the foam sample.

As a result of a strongly heterogeneous stress fields, strong heterogeneities in the development of plastic strain arise. The left column of Fig. 7 provides the fields of the cumulative viscoplastic strain v_{diff} (see Eq. (2)) at two different creep times. The variable v_{diff} results from the time integration of the second equation in (2). It also represents a cumulative norm of the diffusion viscoplastic strain tensor:

$$\dot{v}_{\text{diff}} = \sqrt{\frac{2}{3}\dot{\underset{\sim}{\boldsymbol{\varepsilon}}}^{\text{v}}_{\text{diff}} : \dot{\underset{\sim}{\boldsymbol{\varepsilon}}}^{\text{v}}_{\text{diff}}} \tag{7}$$

Most of viscoplastic deformation is shown to take place in the struts, whereas junctions remain essentially undeformed. Localization of viscoplastic strain close to the ends of several struts reveal a shear deformation of some beams (see for instance the central vertical strut in the snapshots). After 4000 s, viscoplastic strain intensifies in the same struts, whereas nodal regions remain mostly undeformed.

4.3. Strain heterogeneities at a high compression stress

The virtual metallic foam sample is now subjected to a rather large overall compressive stress level of 0.97 MPa at the temperature of 900 °C. The complex architecture of the foam again leads to a complex distribution of stresses inside the struts and the nodes of the cells. The right columns of Figs. 8 and 9 give the histogram distribution of the von Mises equivalent stress at all Gauss points of the nickel mesh. It appears that the high overall load generates equivalent stresses with a mean value of about 36 MPa, at the first time step, in the metal with a large variance. The mean value decreases to around 30 MPa after a 50-s creep due to relaxation in some parts of the foam. A remarkable feature is that a bimodal distribution of stresses is observed with a small bump around 5 MPa and a large one above 30 MPa. It means that most parts of the foam undergo stress levels in the domain of dislocation creep according to the creep behaviour of pure nickel, as shown in Fig. 2. A smaller part is subjected to diffusional creep. As a result of the heterogeneous microstructure of foams, all parts of the foam cannot be in general in the pure dislocation creep regime and the overall response is then a mixture of both material behaviours. Most stress relaxation is observed for the higher stress level, whereas the zones of low stress level do not significantly evolve during creep.

As a result of a strongly heterogeneous stress fields, strong heterogeneities in the development of plastic strain arise. The left columns of Figs. 8 and 9 provide the fields of the cumulative viscoplastic strain v_{disl} (see Eq. (3)) at two different creep times. The variable v_{disl} results from the time integration of the second equation in (3). It also represents a cumulative norm of the dislocation induced viscoplastic strain tensor:

$$\dot{v}_{\text{disl}} = \sqrt{\frac{2}{3}\dot{\underset{\sim}{\boldsymbol{\varepsilon}}}^{\text{v}}_{\text{disl}} : \dot{\underset{\sim}{\boldsymbol{\varepsilon}}}^{\text{v}}_{\text{disl}}} \tag{8}$$

The amount of diffusion creep strain v_{diff} is considerably smaller and not shown in the maps. In comparison to low stress level, viscoplastic strain is found to be more localized in some struts, whereas most of the foam remains almost undeformed. At larger time steps, this tendency to strain localization is confirmed, and large amounts of strain, more than 30%, are reached in some struts. Strain localization mainly takes place in quasi-vertical struts almost parallel to the axial stress load.

Finally, some struts clearly undergo plastic buckling, which is a known failure mechanism in metallic foams under creep [11,13]. A global instability then occurs in the form of a starting crushing band at the lower left part of the sample after 50 s, see the bottom left of Fig. 9. The cells in this region start closing due to the buckling failure of several struts.

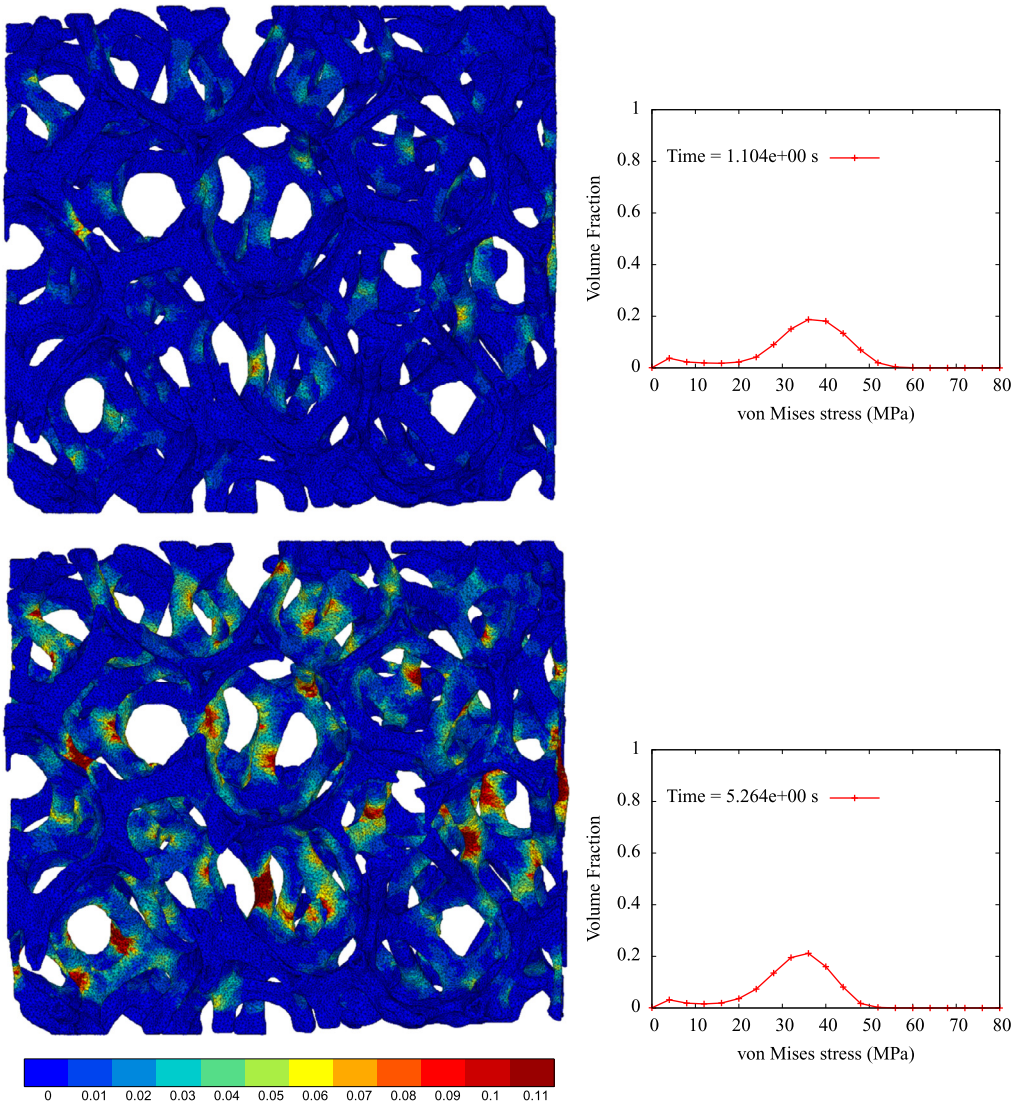

Fig. 8. (Colour online.) Field of cumulative plastic strain v_{disl} (left) inside the foam sample, and distribution of the equivalent von Mises stress within the foam (right) for a compression creep stress $\sigma = 0.97$ MPa applied to the foam. The top and bottom rows correspond to the creep time steps $t = 1.1$ s and $t = 5.3$ s respectively.

5. Discussion

The discussion is focused on the relation between the previous full-field finite-element computations and the overall material response. The computed overall creep strain curves as functions of time are given in Fig. 10 for the two stress levels studied in the two previous subsections. They are compared to the corresponding experimental results in both cases. It appears that the finite-element model is unable to capture the primary creep behaviour observed in the experiment at low stress. In contrast, the creep rate is correctly predicted at the low and high stress levels. The finite-element simulation at high stress predicts an early tertiary creep behaviour due to the formation of a crushing band induced by local viscoplastic buckling. In the experiment, this phenomenon occurs significantly later. This may be attributed to the fact that the foam sample considered for computation is too small.

The latter result raises the question of representativity of the considered sample size to predict the overall behaviour. It has been shown in [26] that samples containing 1, 8 or 24 cells provide very close overall elastic–plastic tensile curves at low temperature, indicating that small-volume elements can be considered as representative to account for the nonlinear material properties of metallic foams. A different conclusion was reached for elastic properties, which seem to require large volume elements to get precise enough elastic moduli [22,25]. We expect that the volume size considered in the present work is sufficient to predict representative overall creep rates, as suggested by the good agreement with experimental results. However, more systematic work is needed to compare the responses of volume elements containing more and more

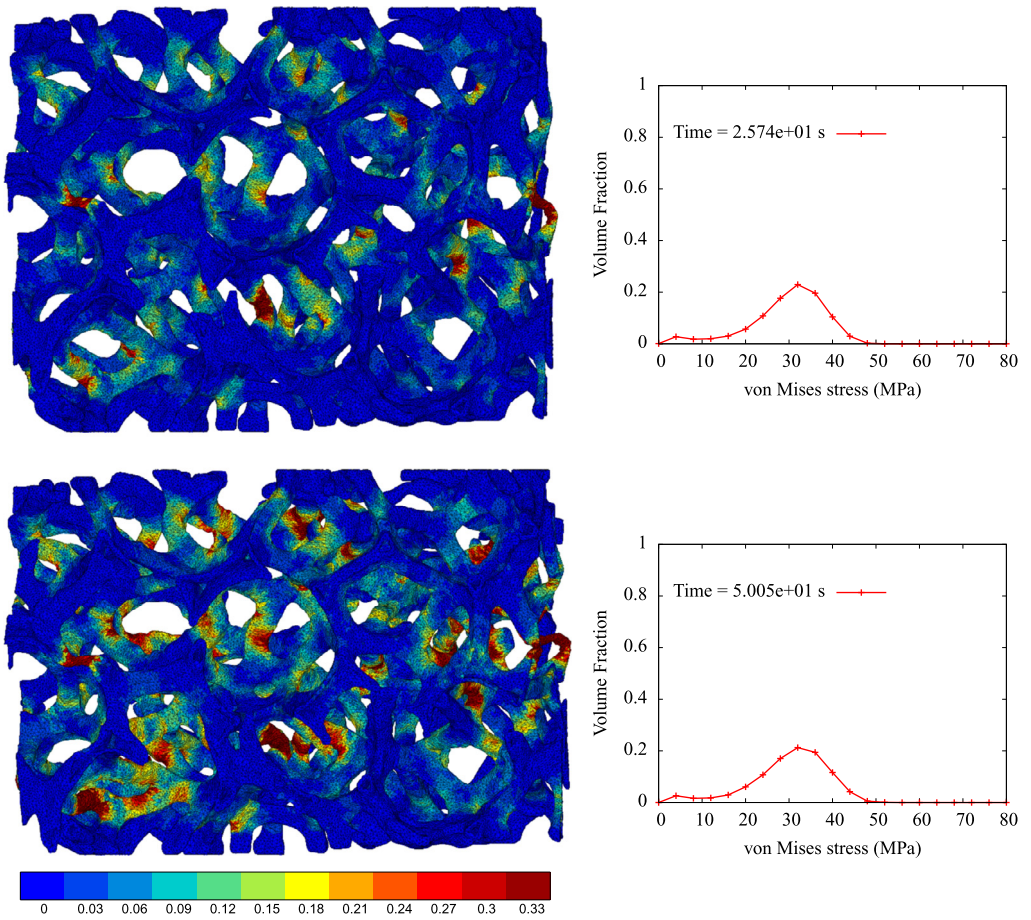

Fig. 9. (Colour online.) Field of cumulative plastic strain v_{disl} (left) inside the foam sample, and distribution of the equivalent von Mises stress within the foam (right) for a compression creep stress $\sigma = 0.97$ MPa applied to the foam. The top and bottom rows correspond to the creep time steps $t = 25.7$ s and $t = 50$ s, respectively.

cells. In particular, the question of representative volume size may be more difficult for the prediction of localization and failure modes of metallic foams, since incipient localization is sensitive to defects and free boundary effects, which are dominant in small volumes. This may explain why the cell-crushing mode predicted by the computation of Section 4.3 occurs too early compared to the experimental result.

The fields of viscoplastic strain as predicted by the simulations can be compared to the overall value. At low stress, after 4000 s, Fig. 7 shows that strain values larger than 1% are to be found in many heavily deformed quasi-vertical or inclined struts that are responsible for most of the foam deformation. Large parts of the foam remain almost undeformed. The corresponding overall strain can be read from Fig. 10(top) and is found to be 1.2% after 4000 s. This overall strain is carried mostly by the heavily deformed struts, and probably also by large rotation effects due to strut bending.

The situation is very different for large creep stresses. Fig. 9(top) shows that after 25 s, several struts are strongly deformed by more than 15% and thus are responsible for the high overall creep strain, 12%, of the foam.

The overall creep results can also be compared to predictions based on available simple homogenization models. As an example, Ashby predicts the following scaling laws for the creep strain rate as a function of stress and relative density:

$$\dot{\varepsilon}^{\star} = \frac{C}{n_s + 2}\left(\frac{(2n_s+1)}{n_s}\right)^{n_s}\sigma^{n_s}\left(\frac{\rho_s}{\rho^{\star}}\right)^{\frac{3n_s+1}{2}} \tag{9}$$

In particular, the Norton exponent $n^{\star}$ of the foam is found to be equal to the one of the pure metal n_s [1]. The model in fact assumes that only one creep mechanism is active in the foam. This is a limitation of the model, since the finite-element computations show that for large enough overall stress levels, both diffusional and dislocation creep mechanisms are active in the foam due to the strong heterogeneous distribution of stress. The coefficient C in the previous formula has been calibrated from the experimental results of this work. For that purpose, we have taken $n_s = 1$ for $\sigma \leq 0.24$ MPa and $n_s = 4$ for $\sigma > 0.24$ MPa. The comparison between Ashby's model and experimental results is shown in Fig. 11. The experiments show a more progressive transition from the diffusion to the dislocation creep regime, even though Ashby's simple approximation

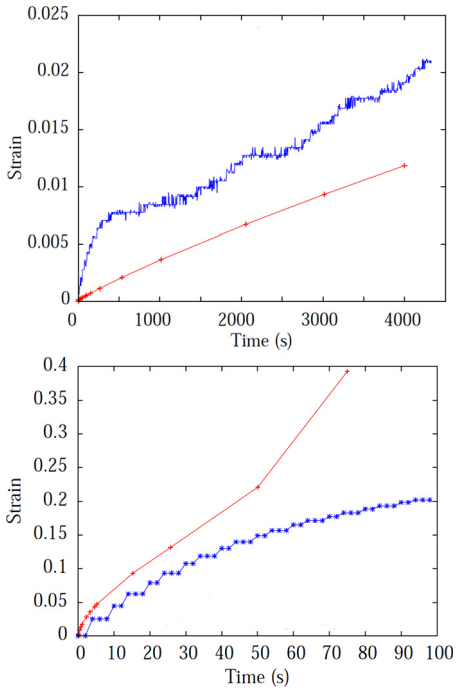

Fig. 10. (Colour online.) Overall creep strain curves as functions of time for the creep stress values $\sigma = 0.12$ MPa (top) and $\sigma = 0.97$ MPa (bottom). The irregular curves correspond to the experimental results, whereas the smooth curves give the simulated results.

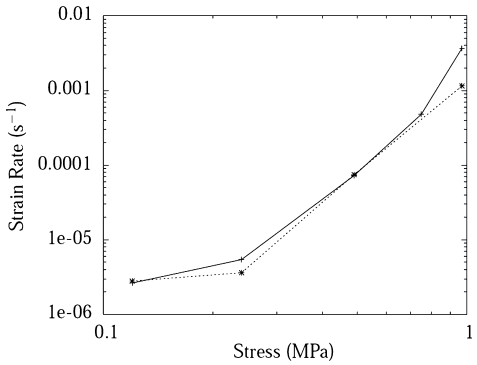

Fig. 11. Creep strain rate according to the stress level at 900 °C. The dotted line corresponds to the identified Ashby model, whereas the experimental results of the this work are given by the continuous line.

remains acceptable. Note also that the Norton exponent in the separate diffusion and dislocation regimes of the foam are the same as for pure nickel according to Table 1, in accordance with formula (9), except at 900 °C where we find $n^\star = 4$ whereas $n_s = 6.6$ at high stress level.

Ashby's model is based on a bending mechanism for the deformation of struts. However, a more complete experimental analysis on nickel-based superalloy foams conducted in [18], shows that Dunand's foam creep model turns out to be more accurate than Ashby's previous model. Dunand's model is based on a compression mechanism of vertical struts [40]. This fact may be supported by some finite-element results in Section 4 showing that many quasi-vertical struts take over most of the creep strain, as visible for instance in the bottom of Fig. 7.

More sophisticated effective modelling of metallic foams based on variational estimates in homogenization theory can be found in [6]. The variational methods developed for viscoplastic composite materials are particularly well-suited for modelling the creep behaviour of foams.

6. Conclusion

Micromechanical modelling of metallic foams based on finite-element simulations from 3D microtomographic images was applied in this work to predict the compression creep behaviour of nickel foams. For that purpose, a virtual foam sample was designed starting from images of the precursor PU foam so that the relative density of the foam can be adjusted to the

specific material studied experimentally. This method can be regarded as a new micromechanical design tool to investigate and improve the behaviour of foams by modifying the density or the shape of cells by means of proper deformation of the initial image, as proposed in [26]. The knowledge about pure nickel creep behaviour available in the literature is sufficient to predict the creep response provided that both diffusional and dislocation creep mechanisms are incorporated in the constitutive model of the foam constituent.

The finite-element simulations of compressive creep on a rather small volume element containing a few dozens of cells are in good agreement with the experimental results in terms of overall strain rate. The experiments were performed in vacuo at three different temperatures and various stress levels.

For large enough overall stress values, the finite-element simulations show a bimodal distribution of stress distribution and strain rate inside the foam. Most deformation is carried by struts quasi-aligned with the overall load direction, whereas most junctions remain almost undeformed or undergo diffusional creep. This is a specific feature of the studied nickel foam characterized by rather short struts and massive nodes. The computational approach confirms that viscoplastic buckling is the main failure mechanism leading to the crushing of cells and associated with tertiary creep.

The computational method can be extended, on the one hand, to more complex loading conditions like multiaxial creep [27] or cyclic creep [41], and, on the other hand, to metallic alloys like superalloy foams, as initiated in [42,18] for Diesel particle filtering applications. Such engineering applications require metal foams with sufficient oxidation resistance [43].

The cellular microstructure plays a major role in the failure mechanisms of the material by controlling the localization modes. Macroscopic models able to capture such strain localization phenomena rely on generalized continuum theories including intrinsic length scales identified from the 2D and 3D field measurements based on microtomographic images, as proposed in [44,45,26].

Acknowledgements

The authors thank Dr. D. Naumann and Dr. S. Saberi from INCO Special Products at that time for constant scientific and financial support of the work.

References

[1] L.J. Gibson, M.F. Ashby, Cellular Solids, Cambridge University Press, 1998.
[2] O. Couteau, D.C. Dunand, Creep of aluminum syntactic foams, Mater. Sci. Eng. A 488 (2008) 573–579.
[3] F. Diologent, Y. Conde, R. Goodally, A. Mortensen, Microstructure, strength and creep of aluminium–nickel open cell foam, Philos. Mag. 89 (2009) 1121–1139.
[4] S. Soubielle, F. Diologent, L. Salvo, A. Mortensen, Creep of replicated microcellular aluminium, Acta Mater. 59 (2011) 440–450.
[5] E.W. Andrews, L.J. Gibson, The role of cellular structure in creep of two-dimensional cellular solids, Mater. Sci. Eng. A 303 (2001) 120–126.
[6] R. Mueller, S. Soubielle, R. Goodall, F. Diologent, A. Mortensen, On the steady-state creep of microcellular metals, Scr. Mater. 57 (2007) 33–36.
[7] S.M. Oppenheimer, D.C. Dunand, Finite element modeling of creep deformation in cellular metals, Acta Mater. 55 (2007) 3825–3834.
[8] R.K. Oruganti, A.K. Ghosh, FEM analysis of transverse creep in honeycomb structures, Acta Mater. 56 (2008) 726–735.
[9] V. Marcadon, F. Feyel, Modelling of the compression behaviour of metallic hollow-sphere structures: about the influence of their architecture and their constitutive material's equations, Comput. Mater. Sci. 47 (2009) 599–610.
[10] V. Marcadon, Mechanical modelling of the creep behaviour of hollow-sphere structures, Comput. Mater. Sci. 50 (2011) 3005–3015.
[11] A.C.F. Cocks, M.F. Ashby, Creep-buckling of cellular solids, Acta Mater. 48 (2000) 3395–3400.
[12] T.J. Chen, J.S. Huang, Creep-rupturing of open-cell foams, Acta Mater. 56 (2008) 2283–2289.
[13] T.J. Chen, J.S. Huang, Creep-buckling of open-cell foams, Acta Mater. 57 (2009) 1497–1503.
[14] T. Theile, H. Loewe, T.C. Theile, M. Schneebeli, Simulating creep of snow based on microstructure and the anisotropic deformation of ice, Acta Mater. 59 (2011) 7104–7113.
[15] X. Badiche, S. Forest, T. Guibert, Y. Bienvenu, J.-D. Bartout, P. Ienny, M. Croset, H. Bernet, Mechanical properties and non-homogeneous deformation of open-cell nickel foams: application of the mechanics of cellular solids and of porous materials, Mater. Sci. Eng. A 289 (2000) 276–288.
[16] T. Dillard, F. Nguyen, É. Maire, S. Forest, Y. Bienvenu, J.-D. Bartout, M. Croset, L. Salvo, R. Dendievel, P. Cloetens, 3D quantitative image analysis of open-cell nickel foams under tension and compression loading using X-ray microtomography, Philos. Mag. 85 (2005) 2147–2175.
[17] V. Goussery, Y. Bienvenu, S. Forest, A.-F. Gourgues, C. Colin, J.-D. Bartout, Grain size effect on the mechanical behavior of open-cell nickel foams, Adv. Eng. Mater. 6 (2004) 432–439.
[18] M. Duchamp, J.D. Bartout, S. Forest, Y. Bienvenu, G. Walther, S. Saberi, A. Boehm, Mechanical behavior of nickel base foams for diesel particle filter applications, in: H. Zhao, N.A. Fleck (Eds.), IUTAM Symposium on Mechanical Properties of Cellular Materials, in: IUTAM Bookseries, vol. 12, 2009, pp. 51–67.
[19] Y. Boonyongmaneerat, D.C. Dunand, Effects of strut geometry and pore fraction on creep properties of cellular materials, Acta Mater. 57 (2009) 1373–1384.
[20] H.S. Zurob, Y. Bréchet, Effect of structure on the creep of open-cell nickel foams, J. Mater. Sci. 40 (2005) 5893–5901.
[21] J.D. DeFouw, D.C. Dunand, Processing and compressive creep of cast replicated IN792 Ni-base superalloy foams, Mater. Sci. Eng. A 558 (2012) 129–133.
[22] É. Maire, A. Fazékas, L. Salvo, R. Dendievel, S. Youssef, P. Cloetens, J.M. Letang, X-ray tomography applied to the characterization of cellular materials. Related finite element modeling problems, Compos. Sci. Technol. 63 (2003) 2431–2443.
[23] A.H. Benouali, L. Froyen, T. Dillard, S. Forest, F. Nguyen, Investigation on the influence of cell shape anisotropy on the mechanical performance of closed cell aluminium foams using micro-computed tomography, J. Mater. Sci. 40 (2005) 5801–5811.
[24] S. Youssef, É. Maire, R. Gaertner, Finite element modelling of the actual structure of cellular materials determined by X-ray tomography, Acta Mater. 53 (2005) 719–730.
[25] O. Caty, É. Maire, S. Youssef, R. Bouchet, Modeling the properties of closed-cell cellular materials from tomography images using finite shell elements, Acta Mater. 56 (2008) 5524–5534.
[26] A. Burteau, F. N'Guyen, J.D. Bartout, S. Forest, Y. Bienvenu, S. Saberi, D. Naumann, Impact of material processing and deformation on cell morphology and mechanical behavior of polyurethane and nickel foams, Int. J. Solids Struct. 49 (2012) 2714–2732.

[27] Z.G. Fan, C.Q. Chen, T.J. Lu, Multiaxial creep of low density open-cell foams, Mater. Sci. Eng. A 540 (2012) 83–88.
[28] J.D. Bartout, Determination of creep properties of pure nickel foams under compressive stress, Technical report, Centre des matériaux, MINES ParisTech, 2008.
[29] D. François, A. Pineau, A. Zaoui, Mechanical Behaviour of Materials. Volume 1: Micro and Macroscopic Constitutive Behaviour. Solid Mechanics and Its Applications, vol. 180, Springer, 2012.
[30] H.J. Frost, M.F. Ashby, Deformation–Mechanism Maps, the Plasticity and Creep of Metals and Ceramics, Pergamon Press, 1982.
[31] V. Goussery, Caractérisations microstructurale et mécanique de mousses de nickel à cellules ouvertes pour batteries de véhicule hybride, PhD thesis, Ecole des mines de Paris, 2004.
[32] S. Karashim, H. Oikawa, T. Motomiya, Steady-state creep characteristics of polycrystalline nickel in temperature range 500 C to 1000 C, Trans. Jpn. Inst. Met. 10 (1969) 205–215.
[33] E.C. Norman, S.A. Duran, Steady-state creep of pure polycrystalline nickel from 0.3 to 0.55 T_m, Acta Metall. 18 (1970) 723–732.
[34] S. Perusin, B. Viguier, J.C. Salabura, D. Oquab, E. Andrieu, Behaviour of the oxide scale during SEM in situ plastic deformation of pure nickel foil, Mater. Sci. Eng. A 387 (2004) 763–767.
[35] G. Cailletaud, K. Sai, Study of plastic/viscoplastic models with various inelastic mechanisms, Int. J. Plast. 11 (1995) 991–1005.
[36] J. Besson, G. Cailletaud, J.-L. Chaboche, S. Forest, M. Blétry, Non-linear Mechanics of Materials, Solid Mechanics and Its Applications, vol. 167, Springer, ISBN 978-90-481-3355-0, 2009, 433 pp.
[37] C. Liu, A.M. Huntz, J.-L. Lebrun, Origin and development of residual stresses in the Ni–NiO system: in-situ studies at high temperature by X-ray diffraction, Mater. Sci. Eng. A 160 (1993) 113–126.
[38] Z-set package, Non-linear material & structure analysis suite, www.zset-software.com, 2013.
[39] N. Limodin, L. Salvo, E. Boller, M. Suery, M. Felberbaum, S. Gailliegue, K. Madi, In situ and real-time 3D microtomography investigation of dendritic solidification in an Al-10 wt.% Cu alloy, Acta Mater. 57 (2009) 2300–2310.
[40] A. Hodge, D. Dunand, Measurement and modelling of creep in open-cell NiAl foams, Metall. Mater. Trans. A 34 (2003) 2353–2362.
[41] S. Soubielle, L. Salvo, F. Diologent, A. Mortensen, Fatigue and cyclic creep of replicated microcellular aluminium, Mater. Sci. Eng. A 528 (2011) 2657–2663.
[42] H. Choe, D.C. Dunand, Synthesis, structure, and mechanical properties of Ni–Al and Ni–Cr–Al superalloy foams, Acta Mater. 52 (2004) 1283–1295.
[43] H. Choe, D.C. Dunand, Mechanical properties of oxidation-resistant Ni–Cr foams, Mater. Sci. Eng. A 384 (2004) 184–193.
[44] S. Forest, J.S. Blazy, Y. Chastel, F. Moussy, Continuum modelling of strain localization phenomena in metallic foams, J. Mater. Sci. 40 (2005) 5903–5910.
[45] T. Dillard, S. Forest, P. Ienny, Micromorphic continuum modelling of the deformation and fracture behaviour of nickel foams, Eur. J. Mech. A, Solids 25 (2006) 526–549.